Mesoporous Fe$_2$O$_3$–CdS Heterostructures for Real-Time Photoelectrochemical Dynamic Probing of Cu^{2+}

Jing Tang,[†,∥] Jun Li,[†,∥] Yueyu Zhang,[‡,∥] Biao Kong,[†] Yiliguma,[†] Yang Wang,[†] Yingzhou Quan,[†] Hao Cheng,[†] Abdullah M. Al-Enizi,[§] Xingao Gong,[‡] and Gengfeng Zheng*,[†]

[†]Laboratory of Advanced Materials, Department of Chemistry, Collaborative Innovation Center of Chemistry for Energy Materials, Fudan University, Shanghai 200433, China

[‡]Center for Key Laboratory of Computational Physical Sciences, Ministry of Education, State Key Laboratory of Surface Physics, and Department of Physics, Fudan University, Shanghai 200433, China

[§]Department of Chemistry-College of Science, King Saud University, Riyadh 11451, Saudi Arabia

Ⓢ *Supporting Information*

ABSTRACT: A three-dimensional (3D) mesoporous Fe$_2$O$_3$–CdS nanopyramid heterostructure is developed for solar-driven, real-time, and selective photoelectrochemical sensing of Cu^{2+} in the living cells. Fabrication of the mesoporous Fe$_2$O$_3$ nanopyramids is realized by an interfacial aligned growth and self-assembly process, based on the van der drift model and subsequent selective in situ growth of CdS nanocrystals. The as-prepared mesoporous Fe$_2$O$_3$–CdS heterostructures achieve significant enhancement (~3-fold) in the photocurrent density compared to pristine mesoporous Fe$_2$O$_3$, which is attributed to the unique mesoporous heterostructures with multiple features including excellent flexibility, high surface area (~87 m^2/g), and large pore size (~20 nm), enabling the PEC performance enhancement by facilitating ion transport and providing more active electrochemical reaction sites. In addition, the introduction of Cu^{2+} enables the activation of quenching the charge transfer efficiency, thus leading to sensitive photoelectrochemical recording of Cu^{2+} level in buffer and cellular environments. Furthermore, real-time monitoring (~0.5 nM) of Cu^{2+} released from apoptotic HeLa cell is performed using the as-prepared 3D mesoporous Fe$_2$O$_3$–CdS sensor, suggesting the capability of studying the nanomaterial–cell interfaces and illuminating the role of Cu^{2+} as trace element.
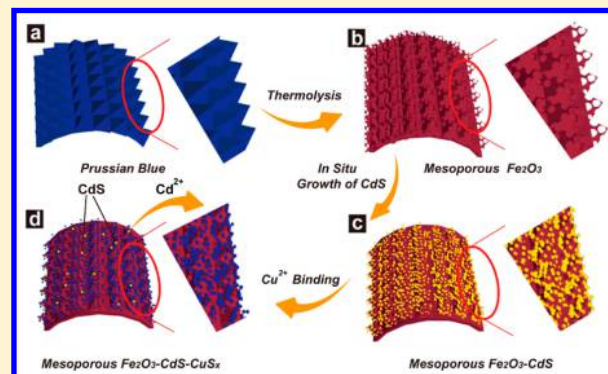
Fundamental cellular functions and medical research have elucidated the function mechanism of many physiological trace elements, which have the potential to greatly improve disease diagnosis.[1−5] Among all the trace elements, copper is an important metal that is essential for most forms of life and the third most abundant transition metal in humans,[6−8] which serves as a structural and catalytic cofactor for many proteins and enzymes such as cytochrome *c* oxidase and copper–zinc superoxide dismutase.[9] Understanding how copper contributes to healthy and disease states requires advanced methods for real-time dynamic probing copper in the living cells rather than in ionic or molecular models.[10] Several methods have been demonstrated to probe Cu^{2+} in biological environments.[11,12] Nonetheless, the ultralow concentrations and complex forms of Cu^{2+} in living cells pose a challenging barrier to monitor the real-time dynamic production and concentration of Cu^{2+} in physiological conditions.[13]

Semiconductor-based photoelectrochemical (PEC) biomolecule detection is a recently developed sensing approach that represents several attractive features.[14−20] First, light and electricity inducers effectively eliminate the signal excitation and detection from the background noise.[21] Second, the

semiconductor nanostructure PEC conversion enables a combination of low intensity light source (such as sunlight) and low electric field for generation of reactive charge carriers and photocurrent, which facilitate the targeted electrochemical reactions without other possible interfering side reactions.[22] Third, compared to conventional electrochemical detections progressing on the electrode surfaces, the PEC method can realize the evolution of oxygen or other reactive oxidative species in the interiors of bulky biomolecules, offering charge relay and efficient signal transducing.[23] Among the semiconductor materials for the PEC conversion, α-Fe$_2$O$_3$ has been demonstrated as one of the most attractive candidates for PEC probing, due to its suitable band gap size (1.9−2.2 eV), photo- and electrochemical stability, nontoxicity, low cost, and earth abundancy.[24−26] Despite these seemingly favorable characteristics, several factors have limited the α-Fe$_2$O$_3$ photoactivity performance,[24] including a short hole diffusion length (2−4

nm) compared with its light penetration depth (~120 nm), short lifetime of charge carriers (~10 ps), and poor mobility of charge carriers (~0.2 cm^2 V^{-1} s^{-1}).[7,27,28] Controlled synthesis of Fe$_2$O$_3$-based heterostructures has been suggested as an attractive approach to improve the separation efficiency of photogenerated electron−hole pairs.[29]

On the other hand, narrow-bandgap semiconductors (e.g., CdS, CdSe, PbS, InP, InAs) have been demonstrated as photosensitizers.[7,30,31] Particularly, CdS is a well-known semiconductor that has been used as a visible-light photosensitizer in PEC conversion, due to its narrow direct band gap (2.4 eV) and flat band potential at 0.66 V (pH 7.0).[32,33] However, as a photocatalyst in aqueous solution, CdS is subject to photocorrosion. As α-Fe$_2$O$_3$ holds lower but closely lying conduction band level and appropriate valence band level with CdS,[27] α-Fe$_2$O$_3$ coupled with CdS can form matched band potentials, which contributes to the stability of CdS. This thermodynamically favored state allows photogenerated electron transfer from the conduction band of CdS to the conduction band of α-Fe$_2$O$_3$ under visible light irradiation, which further enables fast charge separation at the interface of the semiconductor heterostructure and efficient photogenerated carrier reaction at the surfaces. For example, CdS nanowires decorated with α-Fe$_2$O$_3$ nanoparticles were synthesized to show enhanced photocatalytic activity.[34] The Li group utilized double-sided CdS and CdSe quantum dot cosensitized ZnO nanowire arrays for PEC hydrogen generation with a high photoactivity under solar irradiation.[35] Recently, a three-dimensional (3D) aligned mesoporous Fe$_2$O$_3$ has been developed for PEC conversion, due to its large surface area, highly crystalline state, well-aligned frameworks, controllable porosity, and capability of mass synthesis.[36] Nonetheless, to the best of our knowledge, there have been no reports on introducing CdS to 3D mesoporous Fe$_2$O$_3$, which enhances light scattering, charge carrier densities, and effective separation and transport of electron−hole pairs, and more importantly, for the PEC detection of chemical/biological species.[37]

In this paper, a 3D nano-cell interface based on the mesoporous Fe$_2$O$_3$−CdS nanopyramid heterostructure is developed for the solar-driven, real-time, and sensitive PEC probing of physiological levels of trace Cu^{2+} generated by living cells. This process is based on an interfacial charge carrier transfer and tuning mechanism. The 3D mesoporous iron oxide nanopyramids are fabricated by the interfacial thermal decomposition of aligned Prussian blue[36] (Figure 1a,b). Subsequent deposition of CdS nanocrystals on the mesopores of the iron oxide nanopyramids offers significant advantages for increased transfer of photogenerated electrons toward mesoporous Fe$_2$O$_3$ and subsequently much higher photocurrent (Figure 1c) than the unfunctionalized Fe$_2$O$_3$. Afterward, the addition of Cu^{2+} onto the sensor surface can convert CdS to CuS$_x$ (x = 1, 2), owing to the much lower solubility of CuS$_x$.[37−39] The formation of CuS$_x$ on the CdS surface leads to the recombination of excited electrons in the conduction band and holes in the valence band,[37−39] which results in the decrease of photocurrent in the Cu^{2+} solution (Figure 1d). Thus, the main mechanism of this PEC sensor is due to the competitive binding of Cu^{2+} with CdS. The detection indicates an interfacial charge carrier transfer and tuning scheme, and the sensitivity of Cu^{2+} has reached 0.5 nM in buffer, among the best of the previously reported Cu^{2+} sensors.[12,40] Moreover, the 3D mesoporous Fe$_2$O$_3$−CdS sensors have been applied to the real-time monitoring of Cu^{2+} released from HeLa cells, further
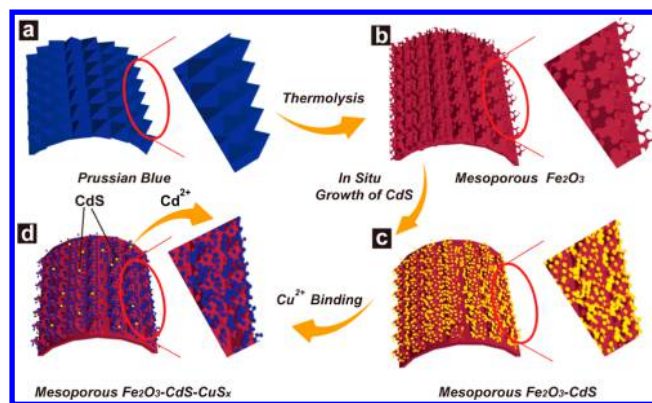

Figure 1. Schematic illustration of synthesis process of (a) 3D aligned Prussian blue nanopyramids, (b) mesoporous Fe$_2$O$_3$ nanopyramids, (c) mesoporous Fe$_2$O$_3$−CdS, and (d) mesoporous Fe$_2$O$_3$−CdS-CuS$_x$.

indicating their potential of investigating the nanomaterial−cell interfaces and exploiting the physiological and pathological roles of Cu^{2+}.

■ EXPERIMENTAL SECTION

Synthesis of 3D Mesoporous Fe$_2$O$_3$. Ti foils (~250 μm thick) with smooth surfaces were utilized as the growth substrates for the hydrolysis of K$_3$[Fe(CN)$_6$].[41] The interfacial growth of Prussian blue on flexible Ti foils and the subsequent in situ thermal conversion led to the formation of 3D mesoporous Fe$_2$O$_3$, according to a previously developed method.[36] In brief, 136 mg of K$_3$[Fe(CN)$_6$]·3H$_2$O was first mixed with 80 mL of hydrochloric acid (0.005 M) under constant stirring for 30 min. Then, a piece of 2 cm × 5 cm Ti foil with smooth surfaces was utilized as the growth substrates and was slowly immersed into the above mixture. Afterward, the container was kept in an oven and heated at 85 °C for 24 h for the hydrolysis of K$_3$[Fe(CN)$_6$].[41] The obtained Prussian blue was taken from the container, washed with deionized (DI) water, and finally dried in a vacuum oven at 55 °C for 12 h. To obtain the 3D mesoporous Fe$_2$O$_3$, the as-made Prussian blue were heated to 450 °C with a temperate ramp of 1 °C min^{-1} for 3 h.

CdS QD Sensitization. 3D mesoporous Fe$_2$O$_3$ were sensitized with CdS QDs, using a chemical bath deposition method.[35] The mesoporous Fe$_2$O$_3$ were dipped into a 0.05 M Cd(NO$_3$)$_2$ ethanol solution for 1 min, rinsed with ethanol, and then dipped for another 1 min into a 0.05 M Na$_2$S methanol solution and rinsed again with methanol. The substrate was then washed with deionized water and air-dried.

Density Functional Theory (DFT) Simulation. In this work, density functional theory (DFT) method was used for structural relaxation and electronic structure calculation. The ion−electron interaction is treated by the projector augmented-wave (PAW) technique, as implemented in the Vienna Ab-initio Simulation Package (VASP). The exchange−correlation potential is treated using the Perdew−Burke−Ernzerhof (PBE) functional. The on-site correlation corrections were included using the Hubbard model (DFT+U approach),[42] and the value of the correlation energy (U) was fixed at 5.0 eV for Fe. The system was simulated by a 3 × 3 four-atomic-layer CdS (0001) surface slab containing 36 atoms upon a 2 × 2 11-atomic-layer α-Fe$_2$O$_3$ surface slab containing 120 atoms. The interface was built as a slab model with vacuum layer 15 Å perpendicular to the surface to avoid the interaction between slabs and the lattice

parameter is 10.28 × 10.28 × 30.77 Å. The 3D k-mesh was generated by the Monkhorst−Pack scheme, where the density of k-points was determined by lattice constant (6 × 6 × 1 for structure relaxation). All atoms were allowed to relax until the net force per atom was less than 0.02 eV/Å and the total electronic extrapolated free energy had converged to less than 0.2 MeV between ionic steps. The antiferromagnetic ground state ordering was taken, corresponding to an AF ++-- state along (0001) in the hexagonal representation with opposite magnetic moments placed on short distance pairs of Fe atoms and equal magnetic moments on larger distance.

Photoelectrochemical Sensing Measurement. Photocurrent was carried out in a three-electrode system, with mesoporous Fe_2O_3−CdS heterostructures photoanode as the working electrode, a coiled Pt wire as the counter electrode, and an Ag/AgCl as the reference electrode. A phosphate buffer saline (PBS, 1×, pH 7.4) was utilized as the electrolyte, with a volume of ~5 mL in an electrochemical cell. Aliquots (volume ~10 μL each time, in PBS buffer) of various Cu^{2+} concentrations were added to the PEC cell. The photoanode was illuminated under 100 mW cm^{-2} simulated sun light. The bias voltage was selected as 0 V (vs Ag/AgCl) to optimize the photocurrent and decrease potential side electrochemical reactions. The solution in the PEC cell was continuously stirred during the whole sensing process to effectively enhance the ion diffusion process.

Real-Time Photoelectrochemical Dynamic Probing of Cu^{2+}. First, the 3D mesoporous Fe_2O_3−CdS was loaded with HeLa cell suspension. After it was incubated for 24 h, it was rinsed with PBS to remove extra HeLa cells from the nanopyramids. The cells on mesoporous Fe_2O_3−CdS were further stained with a fluorescent DNA-binding agent-4′, 6-diamidino-2-phenylindole (DAPI) for facilitating the visualization of the adherent HeLa cells under the Laser Scanning Confocal Microscopy (LSCM) observation. Finally, the chip was placed upside down in a specific dish containing 1 mL of trypsin for the LSCM investigation.

■ RESULTS AND DISCUSSION

The 3D mesoporous Fe_2O_3 nanopyramids were fabricated via first interfacial growth of highly vertically aligned coordination Prussian blue (PB) nanopyramids on the surface of flexible titanium foils via an etching-assisted hydrolysis of precursors. The color of the Ti foil growth substrate changes from silver-white to blue, rust red, and then light yellow (Figure 2a), suggesting the growth of PB, the formation of α-Fe_2O_3, and the deposition of CdS, respectively. In addition, the PB and mesoporous Fe_2O_3 nanopyramids display high flexibility and stable morphology for over 100 times of bending and releasing without observable deformation (Figure S1). The elemental mapping of a representative Fe_2O_3−CdS shows uniform distribution of the Fe, O, Cd, and S signals over the entire substrate (Figure 2b and S2). Scanning electron microscopy (SEM) images show that the smooth surface substrate Ti foils are covered by a layer of nanopyramids (Figure 2c, d). An enlarged SEM image of a single island of mesoporous Fe_2O_3 demonstrates that the PB has been transformed to Fe_2O_3 with obvious mesopores (Figure 2d inset). The side-view SEM images reveal the nanopyramids have a thickness of ~150 nm (Figure S3a, b). The CdS NPs were uniformly deposited on the surface of Fe_2O_3 (Figure 1e and S3c). After incubating with Cu^{2+}, CuS_x NPs were successfully grown on the nanopyramid surface (Figure 1f and S3d). Energy-dispersive X-ray (EDX)
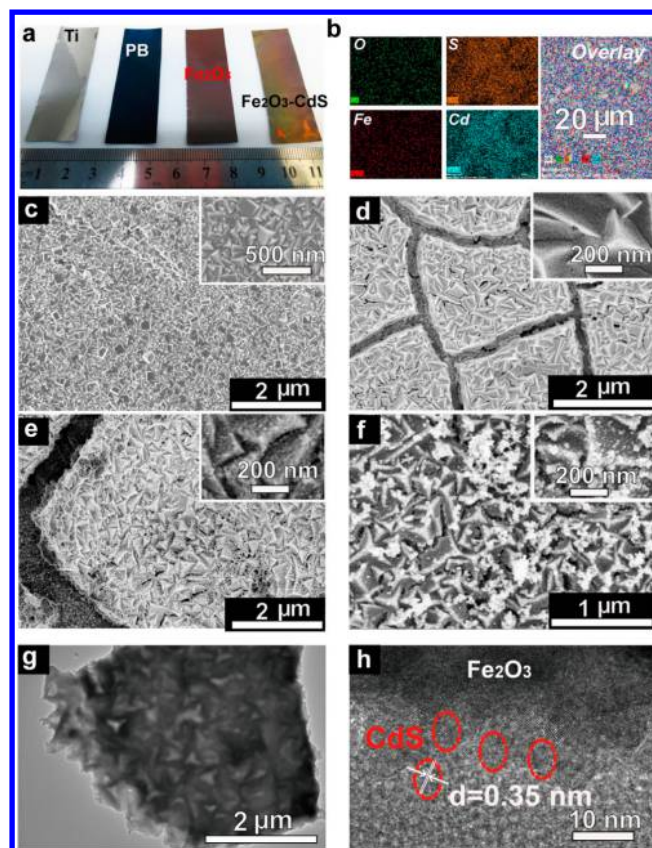

Figure 2. (a) Photographs and corresponding color changes of bare Ti foil substrate (Ti), PB nanopyramids grown on Ti foil (PB), mesoporous Fe_2O_3 on Ti foil after calcination, and Fe_2O_3−CdS. (b) SEM mapping of Fe_2O_3−CdS. (c−f) Low- and (insets) high-resolution SEM images of (c) PB, (d) mesoporous Fe_2O_3, (e) Fe_2O_3−CdS, and (f) Fe_2O_3−CdS-CuS_x. (g) TEM and (h) HRTEM image of Fe_2O_3−CdS.

spectra and mapping of PB (Figure S4), Fe_2O_3 (Figure S5), and Fe_2O_3−CdS-CuS_x (Figure S6) confirm the compositions.

The HRTEM image shows that each PB nanopyramid is solid and crystalline (Figure S7a,b). After CdS QD sensitization, TEM shows the structures of Fe_2O_3−CdS (Figure S8a,b). The mesoporous Fe_2O_3 surface is covered with a number of spherical particles with average diameter of 5−10 nm (Figure 2g). The interplanar spacing is ~0.35 nm, which corresponds to the lattice spacing for the (111) faces of cubic CdS (Figure 2h). X-ray photoelectron spectroscopy (XPS) analysis of the films demonstrates O 1s peak (~533 eV), Fe 2p$_{1/2}$ (~725 eV), and 2p$_{3/2}$ (~710 eV) peaks of Fe_2O_3 (Figure S9), indicating that the examined films mainly contain Fe_2O_3 after thermolysis.[36] The two peaks in Cd 3d core level arise from the spin−orbit interaction, with the Cd 3d$_{5/2}$ peak position at ~404.6 eV and the Cd 3d$_{3/2}$ at ~411.3 eV. The position of the S 2p peak is located at ~160.9 eV, which confirms that S element exists mainly in the form of S^{2-} chemical state on the sample surface.[44] N_2 sorption isotherms of the Fe_2O_3−CdS heterostructures obtained after CdS growth show a high surface area of ~80 m^2 g^{-1}, and a wide pore size distribution centered at ~20 nm (Figure S10).

A three-electrode PEC cell in a PBS (pH 7.4) was employed to explore the PEC biosensing capability of the 3D mesoporous Fe_2O_3−CdS without the molecular targets (Figure S11a). Compared to the photocurrent values of the pristine Fe_2O_3 (0.3

mA cm^{-2}), a dramatically higher photocurrent density of the Fe$_2$O$_3$–CdS photoanode is observed to be ~0.9 mA cm^{-2} at 0 V vs Ag/AgCl under the same simulated sunlight of 100 mW cm^{-2}. The UV–vis reflectance spectra indicate that the Fe$_2$O$_3$–CdS exhibit less reflectance than mesoporous Fe$_2$O$_3$ (Figure S12). The charge carrier densities are subsequently measured by the electrochemical impedance spectroscopy. The mesoporous Fe$_2$O$_3$–CdS shows a much smaller slope in the Mott–Schottky plot, suggesting a higher charge carrier density, compared to the mesoporous Fe$_2$O$_3$ (Figure S11b).[45] These results indicate that the improved photoactivity of the mesoporous Fe$_2$O$_3$–CdS is primarily attributed to the enhanced light absorption and charge carrier transfer of CdS sensitized to mesoporous Fe$_2$O$_3$ surface. These photocurrent densities are highly stable and in good accordance with the on/off cycles of the light illumination (Figure S11c). Furthermore, the photocurrent is well maintained for >94% over 12 h of continuous light illumination (Figure S11d).

The PEC enhancement mechanism of the Fe$_2$O$_3$–CdS heterostructure is further illustrated by density functional theory (DFT) simulation. A slab model is used to build different configuration of the interface between Fe$_2$O$_3$ and CdS (Figure 3a). The Bader method is used to analyze the average
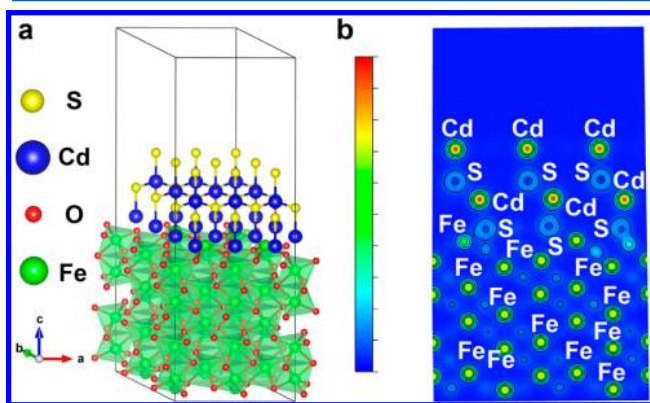

Figure 3. (a) Structure model for simulation of the interface of Fe$_2$O$_3$ and CdS. The green, red, blue, and yellow spheres represent Fe, O, Cd, and S ions/atoms, respectively. (b) The contour plot of the total charge density of the Fe$_2$O$_3$ and CdS interface in the (110) direction.

charge transfer between Fe$_2$O$_3$ and CdS interface.[46] The charge transfer between the interfaces mainly occurs from S to Fe atoms, and the average charge transfer of 0.49 electron per S atom is observed from CdS layer to Fe$_2$O$_3$. The enhanced charge transfer is attributed to the large difference in work functions at the interface of CdS and Fe$_2$O$_3$.[27] To characterize the change of electronic structure at the interface, a two-dimensional contour plot is made between the CdS and the Fe$_2$O$_3$ surface (Figure 3b). A significant charge transfer is observed from the CdS surface to the Fe$_2$O$_3$ surface, implying efficient electron accumulation in Fe$_2$O$_3$. Both the simulation and the aforementioned Mott–Schottky plot measurement (Figure S11b) show that the charge carrier density is higher than that of pure Fe$_2$O$_3$, as well as the Fe$_2$O$_3$–CdS–CuS$_x$ heterostructure.

Before the probing of Cu^{2+} in a solution, the mesoporous Fe$_2$O$_3$–CdS PEC sensor is in the state of "**PEC-ON**", i.e., with a much higher photocurrent value than the pristine mesoporous Fe$_2$O$_3$ (0.9 vs 0.3 mA cm^{-2}) (Figure S11a, red curve). Under the same simulated sunlight illumination, the real-time sensing

experiments of Cu^{2+} are investigated with a small applied bias of 0 V vs Ag/AgCl to minimize the interference of other potentially coexisting reductive species in the solution. The successive additions of Cu^{2+} at intervals in the PEC cell generate well-defined steps of photocurrent decrease each time (Figure 4a). The lowest concentration detectable by the 3D
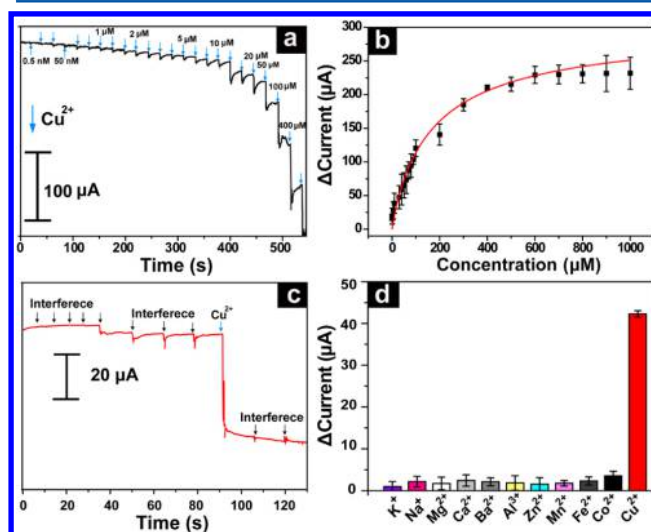

Figure 4. (a) Photocurrent versus time data of a Fe$_2$O$_3$–CdS PEC sensor for consecutive additions of Cu^{2+} (shown by arrows) at 0 V vs Ag/AgCl under sun light illumination. (b) Summary of the sensing signal versus the Cu^{2+} concentration. (c) Photocurrent versus time data of a Fe$_2$O$_3$–CdS PEC sensor for continuous addition of Cu^{2+} (with a final concentration increase of 10 μM each time), and other interference molecules (with an ultimate concentration enhancement of 10 μM each time), designated by the arrows. Photocurrent change of the Fe$_2$O$_3$–CdS PEC sensors at the presence of (d) the metal ion.

mesoporous Fe$_2$O$_3$–CdS sensors is 0.5 nM (Figure S13). Further investigation proves the selectivity of the 3D mesoporous Fe$_2$O$_3$–CdS-based PEC biosensors by measuring the photocurrent response induced by different interference metal ions. The detection performances of the 3D mesoporous Fe$_2$O$_3$–CdS PEC biosensor are summarized and compared with those reported in the literature (Table S1). It is clear that the 3D mesoporous Fe$_2$O$_3$–CdS PEC sensor shows a much higher sensitivity (0.5 nM) and more extended linearity (50 nM-600 μM) than other total Cu^{2+} sensors reported in the literature.

The decrease of the photocurrent level is triggered by the binding of S^{2-} to Cu^{2+}, confirming the quenching of the charge transfer from CdS to 3D mesoporous iron oxide nanopyramids, that is, the "**PEC-off**" state. These low concentrations have been repeatedly tested and have gained featured highly reproducible photocurrent-sensing responses. The photocurrent change is summarized in the corresponding concentration-dependence calibration curves (Figure 4b).

To verify the selectivity of the Cu^{2+} sensor, various metal ions (K$^+$, Na$^+$, Mg^{2+}, Ca^{2+}, Ba^{2+}, Al^{3+}, Zn^{2+}, Mn^{2+}, Fe^{2+}, and Co^{2+}) with 10 μM concentrations were tested. It can be seen that most of these ions do not lead to the photocurrent density change on the Fe$_2$O$_3$/CdS electrode (Figure 4c,d). A slight photocurrent decrease (<5 μA) is observed in Fe^{2+} and Co^{2+}, due to the close solubility product between these sulfides with CdS, in good accord with literatures.[37−39] In contrast, the introduction of the same concentration of Cu^{2+} into the sensor

assay leads to significant photocurrent change, confirming our proposed detection mechanism. As demonstrated above, our approach for Cu^{2+} detection shows high selectivity, suggesting the present PEC sensor can potentially be applied for detecting Cu^{2+} in living biosystems.[37−39]

The capability of the mesoporous Fe_2O_3−CdS PEC sensors for recording of Cu^{2+} release from living cells is further investigated (Figure 5a). In the process, Hela cells were directly
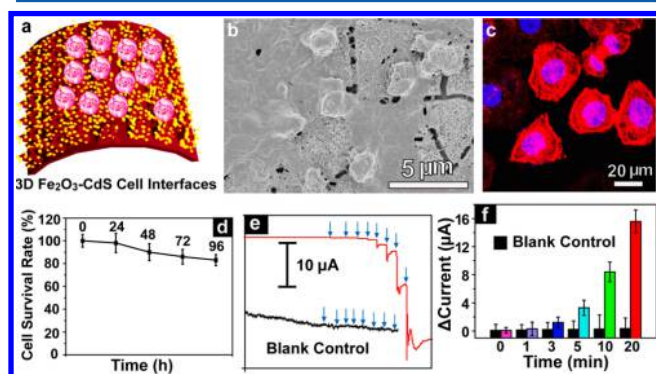

Figure 5. 3D mesoporous nano-cell interfaces for real-time photo-electrochemical dynamic probing of Cu^{2+}. (a) Schematic representation of living cells cultured on Fe_2O_3−CdS. (b) SEM images of fixed Hela cells on Fe_2O_3−CdS films. (c) Fluorescence images of Hela cells cultured on the Fe_2O_3−CdS. The cells were stained with phalloidin-tetramethylrhodamine B isothiocyanate for F-actin (red), 4′,6-diamidino-2-phenylindole dihydrochloride (DAPI) for nuclei (blue). (d) Percentage of viable HeLa cells cultured on the Fe_2O_3−CdS. (e, f) Real-time detection of Cu^{2+} by the Fe_2O_3−CdS PEC sensor, when trypsin was added at different time to the cell culture. A similar PEC sensor but without cell culture was used as the blank control.

cultured on top of the mesoporous Fe_2O_3−CdS arrays to reach the growth confluence, preserving well-conditioned morphologies and tight contact to the mesoporous Fe_2O_3−CdS interfaces judged by SEM images (Figure 5b). Then, fluorescence imaging was employed to observe the living Hela cells, in which F-actins and nuclei were labeled by phalloidin-tetramethylrhodamine B isothiocyanate (red color) and 4′,6-diamidino-2-phenylindole dihydrochloride (DAPI, blue color), respectively (Figure 5c). The Hela cells show normal morphologies, active cell functions and proliferation with its viability retained at >90% and >85% over 24, 48, 72, and 96 h growth on the nanopyramids, respectively, indicating low cytotoxicity of the sensor platform for cell culture (Figure 5d). This phenomenon implies the potential application of 3D mesoporous Fe_2O_3−CdS nanopyramids in real-time and in situ monitoring of the complex Cu^{2+} released from biosystems.

The mesoporous Fe_2O_3−CdS nanopyramid biosensor is further explored for the PEC probing of Cu^{2+} released from living cells. During the digestion and apoptosis processes of cells generated by trypsin, the Cu^{2+} ions (in both free and complex forms) are released,[47] which can be evaluated the 3D mesoporous Fe_2O_3−CdS PEC sensor. The real-time monitoring shows that discrete photocurrent increases are repeated observed upon the corresponding addition of trypsin into the Hela cell culture (Figure 5e,f), indicating the excellent capability of direct culturing and PEC detection of the important cellular molecules by the nanopyramids. It should also be noted that both free and complex Cu^{2+} ions are released from the cells. In order to accurately determine the exact Cu^{2+} concentrations in cells, more detailed calibrations of different

complex forms of Cu^{2+} ions are required with standard samples such as [Cu−Zn] superoxide dismutase,[47] in addition to free Cu^{2+} ions. Furthermore, it is possible that some organic molecule interferences can act as the hole scavengers and affect the PEC signal. However, the charge transfer sensitization between CdS (or CuS_x) and Fe_2O_3 has a much more significant effect on the photocurrent density and the sensing signal. Therefore, our system can still present good selectivity in biological systems. In contrast, Fe_2O_3−CdS without the cells do not show signals, indicating the selectivity of our PEC sensors (Figure 5e,f). The robust sensing performance and long-term function stability of the 3D mesoporous Fe_2O_3−CdS PEC sensor is attributed to the stable structures and optoelectronic performances of CdS sensitizer and 3D mesoporous Fe_2O_3, as well as their strong chemical binding. These results further suggest that the present 3D mesoporous Fe_2O_3−CdS can be further used to detect the Cu^{2+} in various biosystems.

■ CONCLUSIONS

In summary, a sensing platform using 3D mesoporous Fe_2O_3−CdS nanopyramid heterostructure for solar-driven, real-time, and selective photoelectrochemical sensing of Cu^{2+} is developed. Compared to conventional sensing approaches, the 3D mesoporous Fe_2O_3−CdS nanopyramid sensors display several significant advantages, excellent biocompatibility, including effectively reduction of background interference, simplicity, rapid response, excellent flexibility, and low cost for practical bioapplications. This promising sensing platform enables rapid and accurate diagnosis for Cu^{2+} with a low detection limit (∼0.5 nM). Furthermore, the fabrication and investigation of 3D mesoporous nanopyramids provide a new paradigm for fabrication of unconventional solar-driven mesoporous heterostructures and further suggest a new strategy for designing a low-cost and sensitive photoelectrochemical dynamic sensing interface toward living cells.

■ ASSOCIATED CONTENT

⑤ Supporting Information
Supporting figures S1−S13 and Table S1. The Supporting Information is available free of charge on the ACS Publications website at DOI: 10.1021/acs.analchem.5b00844.

■ AUTHOR INFORMATION

Corresponding Author
*E-mail: gfzheng@fudan.edu.cn (G.Z.).
Author Contributions
∥These authors contributed equally (J.T., J.L. and Y.Z.).
Notes
The authors declare no competing financial interest.

■ ACKNOWLEDGMENTS

■ REFERENCES

(1) Fan, R.; Vermesh, O.; Srivastava, A.; Yen, B. K.; Qin, L.; Ahmad, H.; Kwong, G. A.; Liu, C.-C.; Gould, J.; Hood, L. *Nat. Biotechnol.* **2008**, *26*, 1373−1378.

(2) Tian, B.; Lieber, C. M. *Annu. Rev. Anal. Chem.* **2013**, *6*, 31.

(3) Patolsky, F.; Timko, B. P.; Yu, G.; Fang, Y.; Greytak, A. B.; Zheng, G.; Lieber, C. M. *Science* **2006**, *313*, 1100−1104.

(4) Xie, P.; Xiong, Q.; Fang, Y.; Qing, Q.; Lieber, C. M. *Nat. Nanotechnol.* **2012**, *7*, 19−125.

(5) Gao, N.; Zhou, W.; Jiang, X.; Hong, G.; Fu, T.-M.; Lieber, C. M. *Nano Lett.* **2015**, *15*, 2143−2148.

(6) Zeng, L.; Miller, E. W.; Pralle, A.; Isacoff, E. Y.; Chang, C. J. *J. Am. Chem. Soc.* **2006**, *128*, 10−11.

(7) Shi, Y.; Li, H.; Wang, L.; Shen, W.; Chen, H. *ACS Appl. Mater. Interfaces* **2012**, *4*, 4800−4806.

(8) Cotruvo, J. J. A.; Aron, A. T.; Ramos-Torres, K. M.; Chang, C. J. *Chem. Soc. Rev.* **2015**, *44*, 4400−4414.

(9) Domaille, D. W.; Que, E. L.; Chang, C. J. *Nat. Chem. Biol.* **2008**, *4*, 168−175.

(10) Que, E. L.; Chang, C. J. *J. Am. Chem. Soc.* **2006**, *128*, 15942−15943.

(11) Ding, C.; Zhu, A.; Tian, Y. *Acc. Chem. Res.* **2013**, *47*, 20−30.

(12) Zhu, A.; Qu, Q.; Shao, X.; Kong, B.; Tian, Y. *Angew. Chem., Int. Ed.* **2012**, *124*, 7297−7301.

(13) Liu, S. Y.; Qi, X. L.; Lin, R. B.; Cheng, X. N.; Liao, P. Q.; Zhang, J. P.; Chen, X. M. *Adv. Funct. Mater.* **2014**, *24*, 5928−5928.

(14) Zhao, W.-W.; Xu, J.-J.; Chen, H.-Y. *Chem. Soc. Rev.* **2015**, *44*, 729−741.

(15) Zhao, W.-W.; Xu, J.-J.; Chen, H.-Y. *Chem. Rev.* **2014**, *114*, 7421−7441.

(16) Bai, J.; Zhou, B. *Chem. Rev.* **2014**, *114*, 10131−10176.

(17) Zhang, X.; Meng, F.; Mao, S.; Ding, Q.; Shearer, M. J.; Faber, M. S.; Chen, J.; Hamers, R. J.; Jin, S. *Energy Environ. Sci.* **2015**, *8*, 862−868.

(18) Luo, J.; Tilley, S. D.; Steier, L.; Schreier, M.; Mayer, M. T.; Fan, H. J.; Grätzel, M. *Nano Lett.* **2015**, *15*, 1395−1402.

(19) Wang, G.; Ling, Y.; Wang, H.; Yang, X.; Wang, C.; Zhang, J. Z.; Li, Y. *Energy Environ. Sci.* **2012**, *5*, 6180−6187.

(20) Karuturi, S. K.; Luo, J.; Cheng, C.; Liu, L.; Su, L. T.; Tok, A. I. Y.; Fan, H. J. *Adv. Mater.* **2012**, *24*, 4157−4162.

(21) Lu, W.; Wang, G.; Jin, Y.; Yao, X.; Hu, J.; Li, J. *Appl. Phys. Lett.* **2006**, *89*, 263902.

(22) Paracchino, A.; Laporte, V.; Sivula, K.; Grätzel, M.; Thimsen, E. *Nat. Mater.* **2011**, *10*, 456−461.

(23) Tang, J.; Wang, Y.; Li, J.; Da, P.; Geng, J.; Zheng, G. *J. Mater. Chem. A* **2014**, *2*, 6153−6157.

(24) Mayer, M. T.; Lin, Y.; Yuan, G.; Wang, D. *Acc. Chem. Res.* **2013**, *46*, 1558−1566.

(25) Huang, Z.; Lin, Y.; Xiang, X.; Rodríguez-Córdoba, W.; McDonald, K. J.; Hagen, K. S.; Choi, K.-S.; Brunschwig, B. S.; Musaev, D. G.; Hill, C. L. *Energy Environ. Sci.* **2012**, *5*, 8923−8926.

(26) Lin, Y.; Zhou, S.; Sheehan, S. W.; Wang, D. *J. Am. Chem. Soc.* **2011**, *133*, 2398−2401.

(27) Zhang, S.; Xu, W.; Zeng, M.; Li, J.; Xu, J.; Wang, X. *Dalton Trans.* **2013**, *42*, 13417−13424.

(28) Shi, X.-L.; Cao, M.-S.; Yuan, J.; Zhao, Q.-L.; Kang, Y.-Q.; Fang, X.-Y.; Chen, Y.-J. *Appl. Phys. Lett.* **2008**, *93*, 183118−183118.

(29) Li, J.; Cushing, S. K.; Zheng, P.; Meng, F.; Chu, D.; Wu, N. *Nat. Commun.* **2013**, *4*, Articleno. 2651.

(30) Lee, Y.-L.; Chi, C.-F.; Liau, S.-Y. *Chem. Mater.* **2009**, *22*, 922−927.

(31) Cheng, C.; Karuturi, S. K.; Liu, L.; Liu, J.; Li, H.; Su, L. T.; Tok, A. I. Y.; Fan, H. J. *Small* **2012**, *8*, 37−42.

(32) Tada, H.; Mitsui, T.; Kiyonaga, T.; Akita, T.; Tanaka, K. *Nat. Mater.* **2006**, *5*, 782−786.

(33) Li, H.; Cheng, C.; Li, X.; Liu, J.; Guan, C.; Tay, Y. Y.; Fan, H. J. *J. Phys. Chem. C* **2012**, *116*, 3802−3807.

(34) Wang, L.; Wei, H.; Fan, Y.; Gu, X.; Zhan, J. *J. Phys. Chem. C* **2009**, *113*, 14119−14125.

(35) Wang, G.; Yang, X.; Qian, F.; Zhang, J. Z.; Li, Y. *Nano Lett.* **2010**, *10*, 1088−1092.

(36) Kong, B.; Tang, J.; Selomulya, C.; Li, W.; Wei, J.; Fang, Y.; Wang, Y.; Zheng, G.; Zhao, D. *J. Am. Chem. Soc.* **2014**, *136*, 6822−6825.

(37) Shen, Q.; Zhao, X.; Zhou, S.; Hou, W.; Zhu, J. J. *J. Phys. Chem. C* **2011**, *115*, 17958−17964.

(38) Wang, G. L.; Xu, J. J.; Chen, H. Y. *Nanoscale* **2010**, *2*, 1112−1114.

(39) Wang, P.; Ma, X.; Su, M.; Hao, Q.; Lei, J.; Ju, H. *Chem.Comun.* **2012**, *48*, 10216−10218.

(40) Zhang, L.; Han, Y.; Zhao, F.; Shi, G.; Tian, Y. *Anal. Chem.* **2015**, *87*, 2931−2936.

(41) Kong, B.; Tang, J.; Wu, Z.; Selomulya, C.; Wang, H.; Wei, J.; Wang, Y.; Zheng, G.; Zhao, D. *NPG Asia Mater.* **2014**, *6*, e117.

(42) Jin, D.; Matthews, M.; Ensher, J.; Wieman, C.; Cornell, E. *Phys. Rev. Lett.* **1997**, *78*, 764.

(43) Lee, Y.-L.; Chi, C.-F.; Liau, S.-Y. *Chem. Mater.* **2010**, *22*, 922−927.

(44) Xu, F.; Yuan, Y.; Han, H.; Wu, D.; Gao, Z.; Jiang, K. *CrystEngComm* **2012**, *14*, 3615−3622.

(45) Wang, Y.; Zhang, Y.-Y.; Tang, J.; Wu, H.; Xu, M.; Peng, Z.; Gong, X.-G.; Zheng, G. *ACS Nano* **2013**, *7*, 9375−9383.

(46) Tang, W.; Sanville, E.; Henkelman, G. *J. Phys.: Condens. Matter* **2009**, *21*, 084204.

(47) Miao, R.; Mu, L.; Zhang, H.; She, G.; Zhou, B.; Xu, H.; Wang, P.; Shi, W. *Nano Lett.* **2014**, *14*, 3124−3129.